CHAPTER 4

RESULTS AND DISCUSSION

It is noted that the flow characteristics associated with the air jet impinging onto the heated disk confined in the cylindrical chamber under investigation are affected by the jet inertia, buoyancy force due to the heated disk, and the geometry of the chamber including the injection pipe diameter and jet-disk separation distance. In the present experiment the injection pipe diameter is fixed at 10.0 mm and the chamber is at the atmospheric pressure. Three jet-disk separation distances are considered with H = 40.0, 50.0, and 60.0 mm for the jet flow rate ranging from 0 to 12.0 slpm (standard liter per minute) and the temperature difference between the disk and the air injected into the chamber is varied from 0 to 25.0℃. As noted in chapter 3, the dimensionless groups governing the flow are the ratio of the jet-disk separation distance to the injection pipe diameter, jet Reynolds number and Rayleigh number. They are respectively defined as

$$HD_j = \frac{H}{D_j} \tag{4.1}$$

$$Re_j = \frac{V_j D_j}{\nu} = \frac{4}{\pi} \frac{Q_j}{\nu D_j} \tag{4.2}$$

$$Ra = \frac{g\beta\Delta T H^3}{\alpha\nu} \tag{4.3}$$

The Grashof number is defined as

$$Gr = \frac{g\beta\Delta T H^3}{\nu^2} = Ra/Pr \tag{4.4}$$

Thus the nondimensional jet-disk separation distance HD_j ranges from 4 to 6, the jet Reynolds number Re_j from 0 to 1,623, the Rayleigh number Ra from 0 to 507,348, and the Grashof number Gr from 0 to 704,783. In what follows selected flow photos

taken from the side views and the measured temperature data are examined closely to delineate how the gas flow characteristics are affected by the jet-disk separation distance in the cylindrical chamber. The results from the present study for $HD_j = 4$ to 6 will be compared with those in the previous study [16] for $HD_j = 1$ to 3.

4.1 Typical Vortex Flow Patterns

At first, the typical steady vortex flow pattern observed in the cylindrical chamber with H=40.0 mm, $\Delta T = 0℃$ and $Q_j = 4.0$ slpm ($HD_j = 4$, Ra = 0, and $Re_j = 541$) at long time when the flow already reaches steady state is illustrated in Fig. 4.1. The steady flow photo from the side view is shown along with the corresponding schematically sketched vortex flow pattern to indicate the actual direction of the flow recirculation, which is based on the detailed flow visualization. The results indicate that there are three circular rolls in the processing chamber. A close inspection of the successive side view flow photos in the video tapes taken during the transient stage of the flow formation reveals that immediately after the impinging, the jet is deflected to move radially outward along the desk and slows down significantly due to the radial spread of the wall-jet flow. The wall-jet flow travels a certain distance from the stagnation point and then moves obliquely upwards as a result of the jet momentum is unable to overcome the wall friction and the retarding effects of the entrained flow in the upper part of chamber. Then, the oblique flow is divided into two streams as it encounters the chamber top. One stream moves radially inwards towards the low pressure region created by the viscous shearing of the surrounding fluid associated with the jet injection, forming the inner roll which is therefore considered as the primary inertia-driven roll. Another stream is defected by the chamber top to move obliquely downwards along the edge of the desk, and finally leaves the chamber through the outlets in the chamber bottom. The outer roll near the sidewall of the

chamber is formed by the backflow from the outlets and rotates in the same direction as the primary inertia driven roll, which is called the corner roll. Furthermore, a smaller third roll which exists in the region between the primary inertia-driven roll and corner roll is found to be induced through the viscous shearing effects produced by the stronger and larger primary inertia-driven roll, which is termed as the secondary inertia-driven roll and has the opposite rotating direction with the primary inertia-driven roll.

Then, the typical long time flow patterns prevailed at higher jet Reynolds numbers(Re_j = 947) are illustrated in Fig. 4.2 with Q_j = 7.0 slpm and $\Delta T = 0°C$ for two jet-disk separation distances at H = 30.0 & 50.0 mm. The results in Fig 4.2(a) for H = 30.0 mm indicate that there are four vortex rolls exist in the chamber. In addition to the primary inertia-driven roll, secondary inertia-driven roll and corner roll already mentioned above, a small circular roll is induced in the region above the primary inertia-driven roll and adjacent to the chamber top, which is found to be induced through the viscous shearing effect by the even stronger and larger primary inertia-driven roll. It is named the tertiary inertia-driven roll which rotates in the opposite direction with the primary inertia-driven roll. It should be noted that at the larger jet-disk separation distance for H=50.0 mm the tertiary inertia-driven roll also appears in the chamber at higher Re_j (Fig. 4.2(b)). But at this larger H the primary inertia-driven roll grows to become relatively large and contacts the sidewall of the chamber and hence it occupies the outer portion of the chamber. Consequently, there is no room available for the corner roll to appear which is somewhat different form that for the smaller H.

Next, when there is a temperature difference between the jet and disk the typical steady vortex flow shown in Fig. 4.3 for H=40.0 mm, $\Delta T = 5.0°C$ and Q_j = 3.0

slpm ($HD_j = 4$, $Re_j = 406$, $Ra = 30,065$ and $Gr/Re_j^2 = 0.26$) is somewhat different

from that in Figs. 4.1 and 4.2 for $\Delta T = 0°C$. Note that only two circular rolls exist in

the chamber. The inner roll is the primary inertia-driven roll as mentioned above and

the outer roll which rotates in the opposite direction with the primary inertia-driven

roll is the buoyancy-driven roll. The buoyancy-driven roll prevails in the outer portion

of the chamber since the local buoyancy-to-inertia ratio at the edge of the disk

Gr/Re_{we}^2 exceeds 33.0 for $HD_j = 1$ and 2 there [16]. Note that the local Reynolds

number for the wall jet flow is defined as $Re_w = \overline{u}H/\nu$ where the average radial

velocity component $\overline{u} = Q_j/(2\pi rH)$. Hence $Re_w = Q_j/(2\pi\nu r)$ and the local Reynolds

number for the wall jet flow at the disk edge $Re_{we} = Q_j/(2\pi\nu R_w) = Re_j \cdot (D_j/8R_w)$.

Moreover, $Gr/Re_{we}^2 = (Gr/Re_j^2) \cdot (8R_w/D_j)^2$. It should be noted that at this larger

jet-disk separation distance for H=40.0 mm both the primary inertia-driven and

buoyancy-driven roll are larger and contact with each other. There is no room

available for the appearance of the secondary inertia-driven roll as shown in Fig. 4.4

by comparing the flow recirculations in the chamber for H = 20.0 & 40.0 mm.

4.2 Effects of HD_j on Onsets of Inertia and Buoyancy Driven Vortex Rolls

Here we investigate the onset of the inertia-driven rolls by visualizing the vortex

flow in the chamber at various jet Reynolds numbers for an unheated disk (Ra=0). At

increasing jet Reynolds number, the primary, secondary and tertiary inertia-driven

rolls appear in sequence. Note that the lowest jet flow rate which can be accurately

resolved in the present experimental apparatus is 0.1 slpm. Even at this small Q_j the

primary inertia-driven roll is already seen in the chamber for all jet-disk separation

distances (H=10.0, 20.0, 30.0, 40.0, 50.0, and 60.0 mm) with the disk unheated. The

present data are summarized in Table 4.1 for the onsets of the secondary and tertiary inertia-driven rolls at various jet-disk separation distances. The results suggest that as the jet Reynolds number exceeds certain level the secondary and tertiary inertia-driven rolls appear in sequence which can be seen from the flow photos in Fig. 4.5.

At a small jet-disk separation distance for HD_j increased from 1 to 3 the onset of the secondary inertia-driven roll becomes earlier but the onset is delayed to a higher Re_j at a lager jet-disk separation distance for HD_j raised from 3 to 4. This nonmonotonic variation in the critical Re_j for the onset of the secondary inertia-driven roll at increasing HD_j can be attributed to the unusual change of the secondary inertia-driven roll with HD_j illustrated in Fig. 4.6. The results indicate that for $HD_j \leq 3$ both the primary and secondary rolls get bigger for an increase in HD_j. But for HD_j raised from 3 to 4 both the primary inertia-driven roll and corner roll grow substantially in size and the secondary inertia-driven roll is squeezed to become smaller. Note that the secondary inertia-driven roll is not seen in the chamber for HD_j = 5 and 6, which could be ascribed to the continuous growth of the primary inertia-driven roll with HD_j and it contacts with the corner roll, wiping out the secondary inertia-driven roll. Furthermore, for HD_j = 5 and 6 the secondary inertia-driven roll is not induced in the range of the Q_j tested in the present study, as shown in Figs. 4.7 and 4.8.

The typical pattern of the tertiary inertia-driven roll for HD_j varied from 1 to 6 is shown in Fig. 4.9. The flow is axisymmetric even for the cases without steady state at long time (Figs. 4.5-4.8), and only the side view flow photos at the vertical plane $\theta=0°$ are given here. The data in Table 4.1 indicate that the onset of the tertiary inertia-driven roll takes place at lower Re_j as HD_j increases from 1 to 4. This is simply because the primary inertia-driven roll is stronger at higher HD_j for a given Re_j, which

in turn causes an earlier onset of the tertiary inertia-driven roll. However, the onset of the tertiary inertia-driven roll is delayed to a higher Re_j for HD_j raised from 4 to 5. This is conjectured to result from the fact that a high Re_j only the primary roll is induced in the chamber except for the tertiary roll for $HD_j = 5$ (Fig. 4.10) and the roll nearly occupies the entire chamber and it is more difficult for the tertiary roll to be induced. But it is noted that the onset of the tertiary inertia-driven roll becomes earlier for a stronger primary roll as HD_j is raised further from 5 to 6.

Next, when there is a temperature difference between the jet and disk the buoyancy-driven roll appears in the outer region of the chamber as the jet flow rate Q_j decreased to a certain value so that the buoyancy-to-inertia ratio Gr/Re_j^2 or the local buoyancy-to-inertia ratio at the edge of the disk Gr/Re_{we}^2 exceeds a critical level, which is shown in Fig. 4.11 for various Q_j and H at $\Delta T = 5℃$. The measured critical values for the onset of buoyancy-driven roll for various H are summarized in Table 4.2. The buoyancy roll appears as the jet Reynolds number is below the critical value listed in the table. The data show that the critical Q_j for the onset of buoyancy-driven roll is higher for a higher ΔT, indicating that the buoyancy force is higher at a higher ΔT and the buoyancy-driven roll can appear at a higher Re_j. It is also noted from the table that for H = 20.0 to 40.0 mm the buoyancy-driven vortex roll always appears at higher ΔT even for Q_j is raised to the highest level of 12.0 slpm tested here. Moreover, the buoyancy-driven roll always appears at the intermediate H of 30.0 mm for all ΔT $\geqq 0.5℃$. Figure 4.12 shows that even at $\Delta T = 0.5℃$ and $Q_j = 12.0$ slpm ($Gr/Re_j^2 = 0.0007$, $Gr/Re_{we}^2 = 5.13$) the buoyancy roll appears. Then, we move forward to illustrate the effects of the jet-disk separation distance on the onset of buoyancy-driven vortex roll. It can be seen from Table 4.2 that the critical Gr/Re_j^2 or

$\mathrm{Gr}/\mathrm{Re}_{\mathrm{we}}^2$ for the onset of buoyancy-driven roll remains nearly constant at various ΔT for a given H when H = 10.0 mm & 20.0mm. But the critical buoyancy-to-inertia ratio increases significantly for increase in ΔT or H for a larger jet-disk separation distance with H = 40.0 mm ~ 60.0 mm. We illustrate in Fig. 4.13 that only the primary inertia-driven roll and buoyancy-driven roll exist in the chamber and they are in close contact for H = 30.0 to 60.0mm. So the critical $\mathrm{Gr}/\mathrm{Re}_{\mathrm{j}}^2$ or the critical $\mathrm{Gr}/\mathrm{Re}_{\mathrm{we}}^2$ for the onset of buoyancy-driven roll needs to be higher to overcome the stronger mutual pushing of the two rolls at a higher ΔT. Moreover, at the same ΔT the critical Q_j for the onset of buoyancy-driven roll increases for HD_j raised from 1 to 2 but decreased for HD_j raised from 4 to 6. For instance, the critical Q_j increases from 2.8 slpm to 8.0 slpm for HD_j raised from 1 to 2 but decreases from 9.2 slpm to 5.1 slpm for HD_j raised from 4 to 6 at $\Delta T = 5°C$ (Table 4.2).

In the present study, the primary inertia-driven roll always appears for all jet-disk separation distances with disk heated except for H of 60.0 mm. For instance, the primary inertia-driven roll is not seen for a relative low Q_j of 0.3 slpm at $\Delta T = 10°C$ and H = 60.0 mm ($Re_j = 41$, Ra =202,939, and $\mathrm{Gr}/\mathrm{Re}_{\mathrm{j}}^2 = 176$) in Fig. 4.14. This could be attributed to the large buoyancy force associated with a very high buoyancy-to-inertia ratio. At a slightly higher Q_j of 0.4 slpm a small primary inertia-driven roll appears near the heated disk (Fig. 4.14). The critical Re_j for the onset of the primary inertia-driven roll with the disk heated for various ΔT is summarized in Table 4.3 for $HD_j = 6$.

Based on the present data given in Table 4.3, the onset of the primary inertia-driven roll for H = 60.0 mm with disk heated can be correlated as

$$\mathrm{Re}_j = 38 + 5 \times 10^{-5} \cdot Ra \tag{4.5}$$

with a standard deviation of 7.9% for $101,470 \le Ra \le 507,348$ and $41 \le Re_j \le 68$.

The present data for the onset of the secondary inertia-driven roll with the disk unheated can be correlated as

$$Re_j = 296.8 - 61.3 \times HD_j^2 + 13.8 \times HD_j^3 \qquad (4.6)$$

with a standard deviation of 7.2% for $1 \le HD_j \le 4$ and $108 \le Re_j \le 243$.

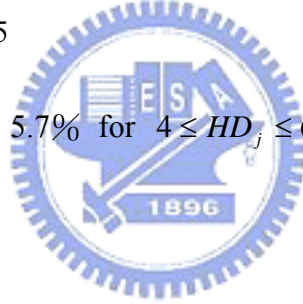The onset of the tertiary inertia-driven roll with the disk unheated can be correlated as

$$Re_j = 1489.3 - 719.5 \times HD_j + 191 \times HD_j^2 - 15.5 \times HD_j^3 \qquad (4.7)$$

with a standard deviation of 5.5% for $1 \le HD_j \le 6$ and $622 \le Re_j \le 947$.

The onset of the buoyancy-driven roll with the disk heated can be correlated as

$$(Gr/ Re_{we}^5)^{0.25} / HD_j^{3.5} = 0.00125 \qquad (4.8)$$

with a standard deviation of 5.7% for $4 \le HD_j \le 6$, $30,065 \le Ra \le 507,348$, and

$811 \le Re_j \le 1,542$.

Finally, we move forward to see the appearance and disappearance of various vortex flow patterns at increasing Re_j. The results in Fig. 4.15 show that there are only primary inertia-driven and corner rolls in the chamber at lower Re_j with the disk unheated for H = 40.0 mm. At increasing Re_j the secondary and tertiary inertia-driven rolls appear in turn. But the corner and secondary inertia-driven rolls are squeezed out by the stronger primary inertia-driven roll when the Re_j is sufficiently high. For higher H of 50.0 and 60.0 mm we also have the primary inertia-driven and corner rolls in the chamber with the disk unheated at small Re_j of 135(Fig. 4.16). At increasing Re_j the corner roll disappears and a further increase in Re_j causes the tertiary inertia-driven roll to appear. These results clearly show the differences in the roll patterns for H

varied from 40.0 to 60.0 mm with the disk unheated. We further examine the change in vortex flow patterns for different H for a heated disk. The results are illustrated in Fig. 4.17 for $\Delta T = 10°C$. Note that at H = 40.0 and 50.0 mm the flow is dominated by the contacting primary and buoyancy rolls at Q_j = 1.0 slpm(Figs. 4.17(a) and (b)). At the very high Q_j of 11.0 and 9.0 slpm the buoyancy roll disappear. But for the high H of 60.0 mm the chamber is dominated by the buoyancy roll at low Q_j of 0.3 slpm and the primary roll is not seen(Fig. 4.17(c)). As increasing Q_j the primary roll appears and occupies the entire chamber at very high Q_j.

4.3 Effects of HD$_j$ on Steady Vortex Flow Characteristics

How the nondimensional jet-disk separation distance affects the gas flow pattern at long time in the chamber with the disk unheated is demonstrated in Figs. 4.18-4.21 by presenting the steady side view flow photos for the cross plane $\theta=0°$ & $180°$ for selected Ra and Re$_j$ at various HD$_j$. First, the results for the disk unheated manifest that at the same Q_j the primary inertia-driven roll is significantly bigger and the corner roll is mildly bigger for an increase in H. But this is not the case for the secondary inertia-driven roll, as already discussed above. It is noted from Fig. 4.20 that as HD$_j$ is raised from 4 to 5 for $\Delta T = 0°C$ and Q_j = 3.0 slpm, the primary inertia-driven roll grows to a large size causing not only the secondary inertia-driven roll but also the corner roll to disappear. The entire chamber is occupied by the primary roll.

Next, the effects of the jet-disk separation distance on the steady vortex flow with the desk heated are exemplified in Fig. 4.22 by showing the steady side view flow photos for $\Delta T = 5°C$ and Q_j = 1.0 slpm at various H. The results clearly indicate that the buoyancy-driven roll which dominates in the outer region of the chamber is much bigger for a larger H. This large increase in the size of the buoyancy-driven roll with the jet-disk separation distance is due to the large increase in the Rayleigh

number associated with a small increase in H since Ra is proportional to H^3, as mentioned above. It is of interest to note that at the larger H (30.0 to 60.0 mm) the radial extent of the buoyancy-driven roll is so large and it directly contacts with the primary inertia-driven roll. Hence the radial extents of the primary inertia-driven and buoyancy-driven rolls are not significantly changed as HD_j is increased from 3 to 4. However, the buoyancy force is much stronger than the inertia force as HD_j is raised from 4 to 6 in such lower Q_j (= 1.0 slpm), which in turn results in the growth of the buoyancy-driven roll and the decay of the primary inertia-driven roll. But the sizes of both the primary inertia-driven roll and buoyancy-driven roll are not significantly changed as HD_j is raised from 3 to 5 at somewhat higher Q_j (2.0 & 3.0 slpm), as shown in Figs. 4.23 and 4.24 for $\Delta T = 5℃$. Similar trends can be seen for other ΔT in Figs. 4.25-4.29.

In addition to the vortex flow characteristics presented above, selected results from the measured steady air temperature distributions in the vortex flow are shown in Fig. 4.30 along a horizontal line at the middle horizontal plane between the disk and chamber top Z=0.5 at θ=0°. The non-dimensional air temperature Φ is defined as $(T-T_j)/(T_f-T_j)$. The air temperature increases slightly with the radial distance measured from the jet axis and reaches a maximum in the region when the wall-jet separates from the disk surface. For a further increase in the radial distance the air temperature starts to decline due to the presence of buoyancy-driven roll and drops sharply near the sidewall of the chamber. A close examination of the data further reveals that at increasing jet-disk separation distance the temperature peak moves toward to the jet axis, reflecting from the fact that we have a smaller primary inertia-driven roll and a larger buoyancy-driven roll for a higher HD_j, as already discussed in Fig. 4.22.

We move further to illustrate how the jet Reynolds number and Rayleigh number affect the long time vortex flow patterns in the chamber with a large H of 40.0 to 60.0

mm. Figure 4.31 shows the cross plane flow photos for Q_j reduced from 3.2 slpm to 0.5 slpm for H = 40.0 mm and $\Delta T = 5℃$. The results clearly show that at decreasing Re_j the primary roll decays significantly accompanying with the growth of the buoyancy roll, which is apparently due to the increase in the buoyancy-to-inertia ratio Gr/Re_j^2 for a fixed ΔT at reducing Re_j. Besides, the primary roll and buoyancy roll are in close contact for all Q_j considerd here and no secondary roll appears in the chamber. Moreover, the results in Figs. 4.32-4.37 for other ΔT and H exhibit a similar trend. It is of interest to point out that at the low Q_j of 0.4 and 0.5 slpm the primary roll is very small and weak and the buoyancy roll is relatively large and strong. The primary roll is somewhat squeezed by the buoyancy roll and does not contact with the chamber top. Finally, the results in Figs. 4.38 and 4.39 for H = 40.0 mm and 50.0 mm at Q_j = 1.0 slpm show that at increasing ΔT the buoyancy roll grows substantially which in turn squeezes the primary roll to become smaller and weaker.
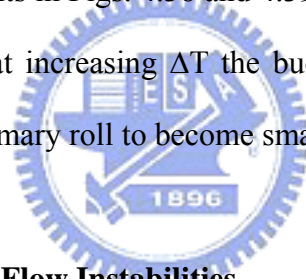
4.4 Effects of HD_j on Vortex Flow Instabilities

For the ranges of the parameters covered in the present and previous studies [26] four types of vortex flow instability are identified in the experiment. They are respectively the inertia-driven vortex flow instability, mutual roll-pushing vortex flow instability, type-1 buoyancy-driven vortex flow instability, and type-2 buoyancy-driven vortex flow instability.

First, the inertia-driven vortex flow instability is found to result from the impinging jet at a sufficiently high jet Reynolds number. At this high Re_j the vortex flow does not reach any steady state at long time. The critical Re_j for the onset of this instability for various ΔT is summarized in Table 4.4 for HD_j = 1 to 6. The results indicate that at small H of 10.0 and 20.0 mm this type of instability exists for all ΔT

examined here. Figures 4.40 and 4.41 show the vortex flow patterns at increasing Re_j for H = 20.0 mm. At certain supercritical Re_j the vortex rolls expand and contact in the radial direction slightly with time, as noted by Hsieh et al. [26]. But for the higher H of 30.0 mm the inertia-driven vortex flow instability only exists for the disk unheated ($\Delta T = 0°C$). For $\Delta T \geqq 5°C$ this flow instability does not appear. The vortex flows associated with this instability for $\Delta T = 0°C$ for H $\geqq$ 30.0 mm are shown in Figs. 4.42-4.45. In Figs. 4.42 and 4.43 for H = 30.0 and 40.0 mm we find that at the high Re_j the primary roll tends to squeeze the secondary and corner rolls to induce flow instability. But for the higher H of 50.0 and 60.0 mm the primary roll oscillates by itself at the supercritical Re_j (Figs. 4.44 and 4.45). Note that for H $\geqq$ 40.0 mm this instability appears for all ΔT considered except for H = 40.0 mm and $\Delta T = 25°C$ (Table 4.4). Selected vortex flow patterns resulting from this instability are illustrated in Figs. 4.46-4.56. We find that for Q_j raised from 9.9 to 10.0 slpm the buoyancy roll near the sidewall of the chamber disappears (Fig. 4.46). It is interesting to note that the primary inertia-driven roll is relatively strong and dominates the flow in the chamber as a result of this high Re_j. Obviously, the unstable vortex flow results from the higher jet inertia and hence it belongs to inertia-driven vortex flow instability. However, the inertia-driven vortex flow instability is not seen in H = 30.0 mm with the disk heated because the buoyancy roll is not weak and small even at small ΔT (Fig. 4.13(c)). Note that the data in Table 4.4 show the increase of the critical Re_j with ΔT for all H, implying that the unsteady flow due to the inertia-driven vortex flow instability can be stabilized by raising the ΔT. The corresponding temporal evolution of the vortex flow in a typical periodic cycle at long time are illustrated in Figs. 4.57-4.60 for selected cases. A close inspection of the data given in Table 4.4 also reveals that for a given ΔT the critical Re_j for the onset of the inertia-driven vortex flow instability is lower when HD_j is raised from 1 to 2 and from 4 to 6, suggesting

31

that the inertia-driven jet flow is less stable at a higher HD_j.

The mutual roll-pushing vortex flow instability is induced only when the jet-disk separation distance is large for H $\geqq$ 30.0 mm. At this H both the primary and buoyancy rolls are large and are in close contact at certain high Re_j and Ra, as already discussed above. Raising Re_j or Ra causes one roll to push the other, resulting the temporal flow oscillation. This is designated as the mutual roll-pushing instability. The associated vortex flow patterns for H = 40.0 mm resulting from this instability are illustrated in Figs. 4.61-4.65 for increasing Re_j at fixed Ra and in Figs. 4.66 and 4.67 for increasing Ra at given Re_j. Similarly trends can be found for H = 50.0 & 60.0mm in Figs. 4.68-4.72. Various flow characteristics on this instability for H = 30.0 mm have been examined in detail by Hsieh et al. [26]. The critical condition for the mutual roll-pushing vortex flow instability is summarized in Table 4.5. The data manifest that an increase in ΔT results in a lower critical Q_j and vice versa a rise in Q_j causes a lower critical ΔT for this instability. It is noted that the vortex flow patterns with the heated disk for H = 40.0 mm given in Fig. 4.73 reveals that the primary inertia-driven roll directly pushes and squeezes the buoyancy-driven roll in certain period of a periodic cycle and in remaining period of the cycle the buoyancy roll pushes back and squeezes the primary roll. Finally, the critical Re_j for the mutual roll-pushing vortex flow instability at fixed ΔT becomes lower for a larger HD_j. But it is not true at large jet-disk separation distance for H = 50.0 mm and 60.0 mm subjected to high ΔT of 20 and 25℃. For these cases no steady state between the mutual roll-pushing vortex flow instability and type-2 buoyancy driven vortex flow instability (this type of instability will be discussed later). And the critical Re_j for the onset of the type-2 buoyancy driven vortex flow instability increases with ΔT(Table 4.6), which results in the delay of the critical Re_j for the onset for the mutual roll-pushing vortex flow instability.

Moreover, the buoyancy-driven vortex flow instability resulting from a high buoyancy-to-inertia ratio Gr/Re_j^2 can be divided into two types. The type-1 buoyancy-driven instability prevailed only for H = 20.0 mm is characterized by the cyclic appearance and disappearance of two additional circular rolls driven by the buoyancy, as shown in Fig. 4.74. These two new rolls are smaller and appear in the middle potion of the chamber right between the inner primary roll and outer buoyancy roll. One comes from the splitting of the primary inertia-driven roll and another from the buoyancy induced new vortex roll. The details of this instability and the associated time-dependent vortex flow are already examined by Hsieh et al. [13].

Finally, the type-2 buoyancy driven vortex flow instability only exists at very low jet Reynolds number for a large jet–disk separation distance with H = 40.0 to 60.0 mm. At this low Re_j the primary inertia driven roll is small and weak and appears near the stagnation region of the impinging jet. Meanwhile, the buoyancy roll is very large and strong, as noted and discussed in section 4.3. As the buoyancy-to-inertia ratio Gr/Re_j^2 exceeds certain critical level, the weak primary roll is squeezed noticeably by the strong buoyancy roll and the vertical dimension of primary inertia-driven roll varies with time. Furthermore, the inner parts of the primary roll can contact and merge with each other at a Re_j much smaller than the critical Re_j for the type-2 buoyancy driven vortex flow instability. A somewhat deformed circular vortice like a deformed chocolate chip is formed right above the heated disk near the jet axis and the jet cannot impinge the heated disk directly. But latter, the centerportion of the vortice is splitted by the impinging jet and it returns to a circular roll. The jet now impinges directly the disk. Thus a cyclic vortex flow pattern evolving between the circular roll and deformed vortice appears, which has not been reported in the literature. Figures 4.75-4.81 show the temporal evolution of this vortex flow patterns

for various ΔT at H = 40.0 to 60.0 mm. It should be mentioned that the vortex flow resulting from this instability is slightly asymmetric and is in a nonperiodic state. No time periodic state is observed in the present study. The critical condition for the onset of the type 2 buoyancy-driven vortex flow instability is summarized in Table 4.6. Note that the critical Gr/Re_j^2 for the type-2 buoyancy-driven instability is much lower for a large H of 50.0 & 60.0 mm.

The presence of multiple vortex flow instabilities in this confined impinging jet flow presented above for H = 40.0 to 60.0 mm indicates that for a moderate temperature difference between the jet and disk the gas flow experiences the inertia-driven instability at sufficiently high Re_j, the mutual roll-pushing instability at intermediate Re_j, and the type-2 buoyancy-driven instability at relatively low Re_j. The vortex flow patterns at selected Re_j covering these three instabilities at certain time instants in the statistical state for H = 40.0 to 60.0 mm are shown in Figs. 4.82-4-95 for various ΔT. Furthermore, vortex flow regime maps delineating the temporal state of the inertia- and buoyancy-driven vortex flow in the chamber are provided in Figs. 4.96-4.98 for various H. It can be concluded from this results that the mutual roll-pushing unstable vortex flow dominates the flow regime map for H = 40.0 mm. As H increases to 50.0 mm the range of the parameter space dominated by the nonperiodic inertia-driven unstable vortex flow gets wider and the nonperiodic mutual roll-pushing unstable vortex flow prevails in a much smaller region. At the larger H of 60.0 mm the range of the nonperiodic inertia-driven unstable vortex flow becomes even wider and the region for the time periodic mutual roll-pushing unstable vortex flow shrinks considerably. Comparing the flow regime maps for H = 10.0 to 30.0 mm shown in Figs. 4.99-4.101 reveals that the region of the stable vortex flow becomes smaller at increasing HD_j which results from both the stronger inertia and buoyancy

driven rolls at a larger HD_j. The present data for the onset of the type-2 buoyancy driven vortex flow instability for H = 40.0 mm can be correlated as

$$\text{Re}_j = 33.6 + 5.2 \times 10^{-7} \times Ra^{1.5} \tag{4.9}$$

with a standard deviation of 10.5％ for $30,065 \le Ra \le 150,325$ and $41 \le \text{Re}_j \le 68$.

The onset of the time periodic mutual roll-pushing vortex flow instability for H = 40.0 mm can be correlated as

$$\text{Re}_j = 591 - 1.17 \times Ra^{0.5} \tag{4.10}$$

with a standard deviation of 12.1％ for $0 \le Ra \le 150,325$ and $149 \le \text{Re}_j \le 568$.

The onset of the nonperiodic mutual roll-pushing vortex flow instability for H = 40.0 mm can be correlated as

$$\text{Re}_j = 1000 - 0.9 \times Ra^{0.5} \tag{4.11}$$

with a standard deviation of 2.1 ％ for $30,065 \le Ra \le 150,325$ and $636 \le \text{Re}_j \le 879$.

The onset of the nonperiodic inertia driven vortex flow instability for H = 40.0 mm can be correlated as

$$\text{Re}_j = 1028 + 1.4 \times Ra^{0.5} \tag{4.12}$$

with a standard deviation of 0.8 ％ for $30,065 \le Ra \le 150,325$ and $1,208 \le \text{Re}_j \le 1,488$.

Then, the onset of the type-2 buoyancy driven vortex flow instability for H = 50.0 mm can be correlated as

$$\text{Re}_j = 84.9 + 5.3 \times 10^{-7} \times Ra^{1.5} \tag{4.13}$$

with a standard deviation of 13.4 ％ for $58,721 \le Ra \le 293,604$ and

$95 \le \mathrm{Re}_j \le 176$.

The onset of the time periodic mutual roll-pushing vortex flow instability for H = 50.0 mm can be correlated as

$$\mathrm{Re}_j = 401.4 - 0.002 \times Ra + 4.5 \times 10^{-9} \times Ra^2 \qquad (4.14)$$

with a standard deviation of 4.7 ％ for $58,721 \le Ra \le 293,604$ and $162 \le \mathrm{Re}_j \le 298$.

The onset of the nonperiodic mutual roll-pushing vortex flow instability for H = 50.0 mm can be correlated as
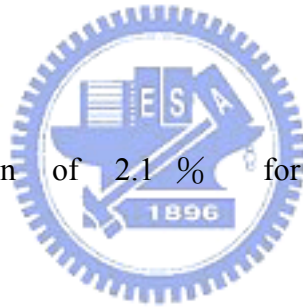
$$\mathrm{Re}_j = 923.7 - 0.536 \times Ra^{0.5} \qquad (4.15)$$

with a standard deviation of 1.7 ％ for $58,721 \le Ra \le 293,604$ and $622 \le \mathrm{Re}_j \le 784$.

The onset of the nonperiodic inertia driven vortex flow instability for H = 50.0 mm can be correlated as

$$\mathrm{Re}_j = 460 + 1.6 \times Ra^{0.5} \qquad (4.16)$$

with a standard deviation of 5.6 ％ for $58,721 \le Ra \le 293,604$ and $920 \le \mathrm{Re}_j \le 1,244$.

Furthermore, the onset of the type-2 buoyancy driven vortex flow instability for H = 60.0 mm can be correlated as

$$\mathrm{Re}_j = 101.7 + 3.9 \times 10^{-7} \times Ra^{1.5} \qquad (4.17)$$

with a standard deviation of 5.1 ％ for $101,470 \le Ra \le 507,348$ and $108 \le \mathrm{Re}_j \le 243$.

The onset of the time periodic mutual roll-pushing vortex flow instability for H = 60.0 mm can be correlated as

$$Re_j = 310.8 - 0.0008 \times Ra + 1.4 \times 10^{-9} \times Ra^2 \tag{4.18}$$

with a standard deviation of 1.7 ％ for $101,470 \leq Ra \leq 507,348$ and $189 \leq Re_j \leq 257$.

The onset of the nonperiodic mutual roll-pushing vortex flow instability for H = 60.0 mm can be correlated as

$$Re_j = 1068 + 1.06 \times Ra^{0.5} \tag{4.19}$$

with a standard deviation of 7.5 ％ for $101,470 \leq Ra \leq 507,348$ and $284 \leq Re_j \leq 690$.

The onset of the nonperiodic inertia driven vortex flow instability for H = 60.0 mm can be correlated as

$$Re_j = 352 + 1.06 \times Ra^{0.5} \tag{4.20}$$

with a standard deviation of 1.7 ％ for $101,470 \leq Ra \leq 507,348$ and $352 \leq Re_j \leq 1,082$.

Finally, the onset of the type-2 buoyancy driven vortex flow instability for $HD_j = 4$ to 6 can be correlated as

$$Re_j = 138.2 - 1807.4 / HD_j^2 + 0.0003 \cdot Ra \tag{4.21}$$

with a standard deviation of 11.3 ％ for $30,065 \leq Ra \leq 507,348$ and $41 \leq Re_j \leq 243$.

The onset of the periodic mutual roll-pushing vortex flow instability for $HD_j = 4$ to 6 can be correlated as

$$Re_j = -54.9 + 38.1 \cdot HD_j + 1.02 \cdot 10^7 / Ra \tag{4.22}$$

with a standard deviation of 10.4 ％ for $30,065 \leq Ra \leq 507,348$ and

$149 \leq \mathrm{Re}_j \leq 446$.

The onset of the nonperiodic mutual roll-pushing vortex flow instability for $HD_j = 4$ to 6 can be correlated as
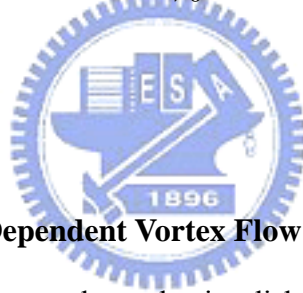
$$\mathrm{Re}_j = 890.4 - 7.9 \cdot HD_j - 0.001 \cdot Ra \tag{4.23}$$

with a standard deviation of 8.2 ％ for $30,065 \leq Ra \leq 507,348$ and $284 \leq \mathrm{Re}_j \leq 879$.

The onset of the nonperiodic inertia driven vortex flow instability for $HD_j = 4$ to 6 can be correlated as

$$\mathrm{Re}_j = -305.6 + 22553.4 / HD_j^2 + 1.14 \times Ra^{0.5} \tag{4.24}$$

with a standard deviation of 8.4 ％ for $30,065 \leq Ra \leq 507,348$ and $352 \leq \mathrm{Re}_j \leq 1,488$.

4.5 Effects of HD$_j$ on Time-Dependent Vortex Flow Characteristics

We move further to illustrate how the jet-disk separation distance affects the mutual roll-pushing time-dependent vortex flow characteristics for the cases at supercritical Re$_j$. As shown in Fig. 4.102 for H = 30.0 mm, $\Delta T = 15℃$ and $Q_j = 5.0$ slpm (Ra = 38,051 and Re$_j$ = 676), the flow photos taken at selected time instants in a typical periodic cycle ($t_p = 1.43$ sec) reveal that the primary inertia-driven roll and buoyancy-driven roll experience the processes of slight growth and decay in a periodic cycle. However, at larger HD$_j$ the oscillation is stronger and the periodic cycle is longer ($t_p = 1.82$ sec for H = 40.0 mm and $t_p = 2.17$ sec for H = 50.0 mm) and becomes nonperiodic for H = 60.0 mm, as evident from the results shown in Figs. 4.103-4.105 at the same ΔT and Q$_j$ when compared with H = 30.0 mm shown in Fig. 4.102. The time records of the nondimensional air temperature Φ defined as

$(T - T_j)/(T_f - T_j)$ at selected locations for the case with Re_j=676 and Ra=90,195 for

H = 40.0 mm are shown in Fig. 4.106. Note that the amplitude of the temperature

oscillation reaches a maximum in the region where the primary and buoyancy rolls

contact with each other. But away from the region the temperature oscillation

decreases significantly. Near the jet axis the temperature oscillation is relatively weak,

as evident from the data for R = 0.17 given in Fig. 4.106(a). Moreover, according to

the power spectrum densities for the time records of Φ, the air temperature measured

at various locations oscillates at the same frequency for the same case (Fig. 4.107).

The data in Fig 4.108 further indicate that at the same Q_j and ΔT the frequency of the

temperature oscillation is lower and the amplitude of the temperature oscillation is

larger, when HD_j is increased from 4 to 6.

From the time records of the nondimensional air temperature for selected

locations for the cases with H = 50.0 mm, $\Delta T = 15.0\,°C$, and Q_j=11.0 slpm shown in

Fig. 4.109, we note that the inertia-driven unstable vortex flow is nonperiodic in time.

The data given in Fig. 4.110 for other HD_j also show that the inertia-driven unstable

flow is nonperiodic. Moreover, we examine the measured instantaneous temperature

data for the inertia-driven unstable flow for Q_j=8.8 to 12.0 slpm at H = 50.0 mm and

$\Delta T = 20.0\,°C$ (based on Table 4.4 the onset of inertia-driven vortex flow for the given

H and ΔT is 8.8 slpm) and find that they are all nonperiodic (Fig. 4.111). In fact, at

larger HD_j = 4 to 6 no time periodic state is found for the inertia driven time

dependent flow except for H = 40.0 mm with the disk unheated, which can be seen in

Table 4.4.

Finally, we illuastrated the type-2 buoyancy-driven unstable vortex flow in Fig.

4.112 by showing the data for the case with H = 50.0 mm, $\Delta T = 15°C$ and Q_j = 0.3

slpm (Ra = 176,162 and Re_j = 47). The temperature data indicate that the vortex flow

is nonperiodic in time. Besides, the flow photos taken at selected time instants also reveal that the vortex flow is nonperiodic. The data given in Fig. 4.113 for other HD_j also show that the type-2 buoyancy-driven unstable flow is nonperiodic. From Table 4.6 the onset of the type-2 buoyancy-driven vortex flow for H = 50.0 mm and $\Delta T = 20.0\,^\circ\!C$ occurs at 1.0 slpm. Tests are conducted for Q_j lowered from 1.0 to 0.2 slpm and no time periodic flow is found (Fig. 4.114). Similar tests were carried out for other H and ΔT and no time periodic state was noted for the type-2 buoyancy-driven unstable vortex flow. The instant flow photos in Figs. 4.75-81 reveals that it takes more time for the inner parts of the primary roll merge with each other for a larger HD_j.

Table 4.1 Critical condition for appearance of the inertia-driven vortex flow
($\Delta T=0^{\circ}C$)

Vortex Roll	Separation distance (H, mm)	Flowrate (Q_j, SLPM)	Re_j
Secondary inertia-driven roll	10.0	1.8	243
	20.0	1.3	176
	30.0	0.8	108
	40.0	1.5	203
	50.0	X	X
	60.0	X	X
Tertiary inertia-driven roll	10.0	5.5	744
	20.0	5.0	676
	30.0	4.6	622
	40.0	4.6	622
	50.0	5.7	771
	60.0	5.2	703

X : The roll does not appear in the range of the parameter tested in the present study.
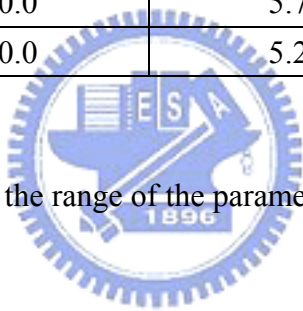
Table 4.2 Critical condition for the onset of the Buoyancy-driven vortex roll for various H.

Separation distance (H, mm)	ΔT (℃)	Flowrate (Q_j, SLPM)	Re_j	Ra	Gr/Re_j^2	Gr/Re_{we}^2
10.0	5.0	2.8	379	470	0.0047	34.9
	10.0	4	541	940	0.0046	34.2
	15.0	5	676	1,409	0.0044	32.9
20.0	5.0	8	1,082	3,758	0.0046	34.2
	10.0	11.4	1,542	7,516	0.0045	33.7
	15.0			◎		
	20.0					
	25.0					
30.0	5.0					
	10.0					
	15.0			◎		
	20.0					
	25.0					
40.0	5.0	9.2	1,244	30,065	0.0277	207
	10.0	9.9	1,339	60,130	0.0479	358
	15.0	10.4	1,407	90,195	0.0651	486
	20.0	10.9	1,474	120,260	0.079	590
	25.0			◎		
50.0	5.0	6.7	906	58,721	0.102	763
	10.0	7.2	974	117,442	0.177	1,321
	15.0	8.0	1082	176,162	0.215	1,605
	20.0	8.7	1,177	234,883	0.242	1,809
	25.0	9.1	1,231	293,604	0.277	2,067
60.0	5.0	5.1	690	101,470	0.305	2,274
	10.0	6.0	811	202,939	0.440	3,286
	15.0	7.0	947	304,409	0.485	3,622
	20.0	7.5	1,014	405,878	0.564	4,207
	25.0	7.9	1,068	507,348	0.635	4,739

◎：The Buoyancy-driven vortex roll always appears in the range of the Q_j tested in the present study.

Table   4.3   Critical condition for appearance of the primary inertia-driven vortex roll at H = 60.0 mm.

Vortex Roll	ΔT ($^\circ$C)	Flowrate (Q_j, SLPM)	Re_j	Ra	Gr/Re_j^2
Primary inertia-driven roll	5.0	0.3	41	101,470	88.0
	10.0	0.4	54	202,939	99.1
	15.0	0.4	54	304,409	149
	20.0	0.4	54	405,878	198
	25.0	0.5	68	507,348	158

Table 4.4 Critical condition for the onset of the inertia-driven time-dependent vortex flow for various H.

Separation distance (H, mm)	ΔT (℃)	Flowrate (Q_j, SLPM)	Re_j	Ra	$(Gr/Re_j^2)\times 10^3$
10.0	0	7.7(9.5)	1,041(1,285)	0	0
	5.0	8.6(9.8)	1,163(1,325)	470	0.495(0.382)
	10.0	8.6(9.9)	1,163(1,339)	940	0.99(0.749)
	15.0	8.7(10.0)	1,177(1,352)	1,409	1.45(1.10)
	20.0	9.0(10.2)	1,217(1,380)	1,879	1.81(1.41)
	25.0	9.3(10.3)	1,258(1,393)	2,349	2.12(1.73)
20.0	0	5.9(8.0)	798(1,082)	0	0
	5.0	6.2(8.3)	839(1,123)	3,760	7.63(4.26)
	10.0	6.6(8.5)	893(1,150)	7,520	13.5(8.12)
	15.0	6.9(8.8)	933(1,190)	11,274	18.5(11.4)
	20.0	7.2(9.0)	974(1,217)	15,033	22.6(14.5)
	25.0	7.3(9.3)	987(1,258)	18,791	27.5(17.0)
30.0	0	5.8(8.9)	784(1,204)	0	0
	5.0 ~ 25.0	X			
40.0	0	4.2(7.6)	568(1,028)	0	0
	5.0	(9.3)	(1,258)	30,065	(27.1)
	10.0	(10.0)	(1,352)	60,130	(47.0)
	15.0	(10.5)	(1,420)	90,195	(63.9)
	20.0	(11.0)	(1,488)	120,260	(77.6)
	25.0	X			
50.0	0	(3.4)	(460)	0	0
	5.0	(6.8)	(920)	58,721	(99.2)
	10.0	(7.3)	(987)	117,442	(172)
	15.0	(8.1)	(1,096)	176,162	(210)
	20.0	(8.8)	(1.190)	234,883	(237)
	25.0	(9.2)	(1,244)	293,604	(271)
60.0	0	(2.6)	(352)	0	0
	5.0	(5.2)	(703)	101,470	(293)
	10.0	(6.1)	(825)	202,939	(426)
	15.0	(7.1)	(960)	304,409	(472)
	20.0	(7.6)	(1,028)	405,878	(549)
	25.0	(8.0)	(1,082)	507,348	(619)

X： The inertia-driven time-dependent vortex flow does not appear in the entire range of the parameter tested in the present study.

( )： The number in the ( ) is the critical value of onset for nonperiodic inertia-driven vortex flow

Table 4.5 Critical condition for the onset of the mutual roll-pushing vortex flow
instability for various H.

Separation distance (H, mm)	ΔT (℃)	Flowrate (Q_j, SLPM)	Re_j	Ra	Gr/Re_j^2
30.0	5.0	5.7(8.4)	771(1,136)	12,684	0.0305(0.0140)
	10.0	5.5(7.9)	744(1,068)	25,367	0.0655(0.0317)
	15.0	5.0(7.4)	676(1,001)	38,051	0.119(0.0543)
	20.0	4.5(7.1)	609(960)	50,735	0.196(0.0786)
	25.0	3.5(7.0)	473(947)	63,418	0.404(0.101)
40.0	5.0	3.3(6.5)	446(879)	30,065	0.216(0.0556)
	10.0	2.2(5.9)	298(798)	60,130	0.97(0.135)
	15.0	1.5(5.5)	203(744)	90,195	3.13(0.233)
	20.0	1.3(4.9)	176(663)	120,260	5.56(0.391)
	25.0	1.1(4.7)	149(636)	150,325	9.7(0.531)
50.0	5.0	2.2(5.8)	298(784)	58,721	0.947(0.136)
	10.0	1.6(5.5)	216(744)	117,441	3.58(0.303)
	15.0	1.4(5.3)	189(717)	176,162	7.02(0.490)
	20.0	1.2(4.9)	162(663)	234,883	12.7(0.764)
	25.0	1.4(4.6)	189(622)	293,604	11.7(1.08)
60.0	5.0	1.8(5.1)	243(690)	101,470	2.45(0.305)
	10.0	1.5(4.7)	203(636)	202,939	7.04(0.717)
	15.0	1.4(3.8)	189(514)	304,409	12.1(1.65)
	20.0	1.6(2.9)	216(392)	405,878	12.4(3.77)
	25.0	1.9(2.1)	257(284)	507,348	11.0(8.98)

( )：The number in the ( ) is the critical value of onset for nonperiodic mutual
roll-pushing vortex flow

Table 4.6 Critical condition for the onset of nonperiodic type-2 buoyancy-driven
time-dependent vortex flow.

Separation distance (H, mm)	ΔT (℃)	Flowrate (Q_j, SLPM)	Re_j	Ra	Gr/Re_j^2
40.0	5.0	0.3	41	30,065	26.1
	10.0	0.3	41	60,130	56.2
	15.0	0.3	41	90,195	78.3
	20.0	0.4	54	120,260	58.7
	25.0	0.5	68	150,325	47.0
50.0	5.0	0.7	95	58,721	9.36
	10.0	0.8	108	117,441	14.3
	15.0	0.9	122	176,162	17.0
	20.0	1.0	135	234,883	18.3
	25.0	1.3	176	293,604	13.6
60.0	5.0	0.8	108	101,470	12.4
	10.0	1.1	149	202,939	13.1
	15.0	1.2	162	304,409	16.5
	20.0	1.5	203	405,878	14.1
	25.0	1.8	243	507,348	12.2